ACS ES&T Water, Volume 6, Issue 1, January 2026, pp. 341–354
DOI: 10.1021/acsestwater.5c01073

Co-removal of cadmium and F-53B from aqueous solutions using montmorillonite-supported sulfidated nZVI: Performance and mechanistic insights

Qing Wang [1#], Yi Zhou [1, 2#], Liangchun Jia [1,3], Frederic Coulon [4], Changxun Dong [3], Bo Zhang [2], Guangwen Zhu [5], Xin Song [1*]

[1] *State Key Laboratory of Soil and Sustainable Agriculture, Institute of Soil Science, Chinese Academy of Sciences, Nanjing 211135, China*

[2] *College of Materials and Advanced Manufacturing, Hunan University of Technology, Zhuzhou 412007, China*

[3] *College of Science, Nanjing Agricultural University, Nanjing, 210095, China*

[4] *School of Water, Energy and Environment, Cranfield University, Cranfield MK43 0AL, UK*

[5] *Shandong Province Leading Green Industry Development Co., Ltd., Jinan, 250199, China*

[*]Corresponding author: Xin Song

Tel.: +86-25-86881543; Fax: +86-25-86881000

E-mail: xsong@issas.ac.cn

Address: No.298 Chuangyou Road, Jiangning District, Nanjing, China.

[#]These authors contributed equally to this work and should be considered co-first authors.

Published by ACS. This is the Author Accepted Manuscript issued with: Creative Commons Attribution License (CC:BY 4.0).
The final published version (version of record) is available online at DOI:10.1021/acsestwater.5c01073. Please refer to any applicable publisher terms of use.

Abstract

The co-contamination of cadmium (Cd) and per- and polyfluoroalkyl substances (PFASs) in water particularly from electroplating industries, poses a significant environmental threat. This study presents the first investigation into the simultaneous removal performance and mechanisms of Cd(II) and chlorinated polyfluoroalkyl ether sulfonate (F-53B, a prevalent PFAS alternative) using montmorillonite-supported sulfidated nano-zero-valent iron (MMT/S-nZVI). The composite exhibited high performance, with maximum sorption capacities of 157.5 mg/g for Cd(II) and 22.3 mg/g for F-53B at 25°C, following pseudo-second-order kinetics. In co-contaminated solutions, MMT/S-nZVI effectively removed simultaneously Cd(II) (50.0 mg/L) and F-53B (1.0 mg/L) under neutral to alkaline conditions, achieving 95.0% Cd(II) and 75.0% F-53B removal at a dosage of 1.0 g/L. A key finding was the asymmetric interaction between contaminants. Cd(II) slightly inhibited F-53B removal, whereas F-53B had minimal effect on Cd(II) removal. Furthermore, MMT/S-nZVI effectively remediated Cd(II) and a mixture of 11 PFASs at environmentally relevant concentrations (μg/L), though removal was more challenging for short-chain compounds. Mechanistic studies revealed that Cd(II) was removed primarily through electrostatic attraction, ion exchange, and precipitation, while F-53B was adsorbed via electrostatic and hydrophobic interactions. These findings provide key insights into the mechanistic interactions for sorbent development to tackle the critical challenge of heavy metal and PFAS co-contamination in water.

Keywords: Sulfidized nZVI; Montmorillonite; Cd(II); F-53B; Co-contaminant; PFASs

Synopsis

MMT/S-nZVI enables efficient co-removal of Cd(II), F-53B, and multiple PFASs at environmentally relevant concentrations, demonstrating potential to remediate heavy metals and PFASs co-contaminated water in field applications.

1 Introduction

Per- and polyfluoroalkyl substances (PFASs) are emerging contaminants of concern due to their persistence, bioaccumulation potential, and health risks [1,2] Perfluorooctane sulfonate (PFOS), a legacy PFASs, has been widely used as a mist suppressant due to its excellent surfactant properties and chemical stability. However, its persistence and toxicity have led to regulatory limits such as the US EPA maximum concentration level (MCL) of 4.0 ng/L [3]. Chlorinated polyfluoroalkyl ether sulfonate (trade name F-53B), a PFOS alternative and dominant mist suppressant in the electroplating industry, has been detected in various environments worldwide, including China, Korea, U.S.A., Europe and Greenland (Arctic) [4–7]. Recent studies reported that the toxicity of F-53B was comparable to, or higher than that of PFOS [3]. Significantly higher concentrations of F-53B were reported near electroplating facilities due to the discharge of wastewater, reaching 43,000-78,000 ng/L in adjacent waters [8] and 742.90 ng/L in treated effluents from an electroplating waste water treatment plant [9]. Cadmium (Cd), a toxic heavy metal commonly used in electroplating processes, is frequently detected in aquatic systems at concentrations far exceeding the World Health Organization (WHO) permissible limit of 3.0 μg/L in drinking water (WHO, 2004) in multiple studies, e.g., 0.003-13700.0 μg/L in surface water [10], 33 μg/L in groundwater [11]. The co-occurrence of Cd and F-53B in water systems raises significant ecological and human health concerns, underscoring the need for treatment strategies capable of simultaneously removing both contaminants.

Sorption is one of the most efficient and cost-effective approaches for the removal of PFASs and heavy metals from aqueous environments [12]. While conventional and novel adsorbents, including activated carbon, biochar, and composite materials, have been applied for pollutant removal [13], most suffer from low capacity, slow kinetics, or focus on single pollutants. The simultaneous removal of co-occurring contaminants such as Cd and PFASs, particularly F-53B, remains a critical gap in water treatment technologies [14].

Nanoscale zero-valent iron (nZVI) is widely used for the removal of environmental pollutants due to its large specific surface area and high reactivity, and environmental benignity[15]. Research has shown that nZVI can remove PFASs and Cd [16,17]. However, its application is limited by oxidation, aggregation, passivation, and restricted electron selectivity [18]. Various strategies have been developed to modify nZVI to overcome its limitations, such as sulfidation (forming S-nZVI), and supporting nZVI on carriers like carbon, biochar, or silica [19]. S-nZVI, typically featuring an Fe-FeS core-shell structure, exhibits improved material stability and enhanced adsorption performance, owing to its increased surface hydrophobicity. It was reported that the removal efficiency of Cd(II) increased remarkably from 14.4% with kaolinite-supported nZVI to 83.97% with S-nZVI, demonstrating the significant enhancement achieved through sulfidation [20]. However, the applicability of S-nZVI for PFASs removal remains limited, with a low removal efficiency of 30% reported for perfluorooctanoic acid (PFOA) [21].

To enhance the removal efficiency for multiple types of pollutants, S-nZVI has been combined with carrier-supported materials [21]. Montmorillonite (MMT), a layered silicate mineral, has been widely used as a supporting material for nZVI due to its environmental friendliness and low cost [19]. MMT possesses an adjustable interlayer spacing of approximately 2-8 Å, which facilitates the accommodation of iron ions and promotes uniform nZVI dispersion [22]. In addition, its abundant surface hydroxyl groups, high ion-exchange capacity, and excellent adsorption properties further enhance its suitability as a support material [19]. Notably, the permanent negative surface charge resulting from isomorphous substitution in MMT's crystal lattice confers a high affinity for cationic pollutants such as Cd(II) [23]. Meanwhile, the layered structure of MMT provides abundant adsorption sites for PFASs through hydrophobic interaction, electrostatic interaction, and hydrogen bonding [24]. Therefore, sulfur modification of nZVI combined with intercalation into MMT interlayers can improve dispersion, reactivity, and stability, while mitigating oxidation [19]. The

successful synthesis of MMT/S-nZVI composites has been reported for the effective removal of pollutants such as trichloroethene [19] and Cr(VI)[25] from aqueous solutions.

To the best of our knowledge, no studies have evaluated the performance of MMT-supported S-nZVI (MMT/S-nZVI) for the simultaneous removal of Cd(II) and F-53B. This study therefore aims to (1) develop an environmentally friendly material with high removal efficiency for the simultaneous removal of Cd(II) and F-53B; (2) evaluate the removal performance of Cd(II) and F-53B co-contamination by MMT/S-nZVI under various influencing factors; (3) assess the efficacy of MMT/S-nZVI for the removal of Cd(II) and the mixture of PFAS compounds at environmentally relevant levels; and (4) investigate the mechanisms for the removal Cd(II) and F-53B by MMT/S-nZVI.

2 Materials and methods

2.1 Chemical reagents

Ferric chloride hexahydrate ($FeCl_3 \cdot 6H_2O$), potassium hydroxide (KOH), potassium nitrate (KNO_3), and sodium chloride (NaCl) were obtained from Sinopharm Chemical Reagent Co., Ltd., China. Sodium borohydride ($NaBH_4$, > 98.0%), Sodium thiosulfate pentahydrate ($Na_2S_2O_3 \cdot 5H_2O$), methanol (CH_3OH) and ammonium acetate (CH_3COONH_4) were purchased from Shanghai Lingfeng Chemical Reagent Co., Ltd., Jiangsu Qiangsheng Functional Chemical Co., Ltd., Merck Chemical Technology (Shanghai) Co., Ltd., and Shanghai Xilong Chemical Co., Ltd., respectively. Acetic acid (CH_3COOH) and nitric acid (HNO_3) were obtained from Nanjing Chemical Reagents and Tianjin Komeo Chemical Reagent Co., Ltd., respectively. 6:2 chlorinated polyfluorinated ether sulfonic acid (F-53B, > 98.0%) was purchased from Sigma-Aldrich (USA), and cadmium chloride ($CdCl_2$) was obtained from Shanghai Jinshan Tingxin Chemical Reagent Factory. Sodium-based montmorillonite (MMT) was supplied by Guzhang Shanlin Shiyu Mineral Products Co., Ltd. All chemicals were analytical grade or higher. Deoxygenated deionized water was prepared by nitrogen purging for 30 min before use.

2.2 Material preparation

The composite MMT/S-nZVI, along with S-nZVI, Fe^{3+}-MMT, and MMT/nZVI, was prepared to compare their sorptive removal behaviors. S-nZVI was synthesized using a co-precipitation method, in which $NaBH_4$ and $Na_2S_2O_3 \cdot 5H_2O$ solutions were added dropwise to a $FeCl_3$ solution under mechanical stirring with nitrogen purging, followed by 30 min of mixing [26]. The molar ratios of Fe^{3+}:BH_4^- and S:Fe were maintained at 1:3 and 3:10, respectively, during the synthesis of S-nZVI. MMT/S-nZVI was then synthesized according to the method of Xu et al. [19], where the molar ratios of Fe^{3+}:BH_4^- and S:Fe were kept the same as those in the preparation of S-nZVI.

The preparation of MMT/S-nZVI began with synthesizing Fe^{3+}-MMT by mixing 50.0 g MMT with 1.0 L $FeCl_3$ (0.1 M) solution under acidic conditions (pH 2-3) for 8 h. Fe^{3+}-MMT was then separated by centrifugation at 10,000 rpm for 20 min. The Fe^{3+} saturation process was repeated 8 times to ensure that the MMT cation exchange sites were fully saturated with Fe^{3+}. Then, the Fe^{3+}-saturated MMT was washed with deionized water to remove Cl^-, followed by freeze-drying. 5.0 g Fe^{3+}-MMT powder was suspended in 20.0 mL deionized water. The suspension was then reduced to MMT/nZVI through dropwise addition of excess $NaBH_4$ (1 mL/min) under N_2 atmosphere with mechanical stirring for 60 min. The suspension color changed from dark yellow to ochre during this process, a red earth color. Afterward, 0.045 g $Na_2S_2O_3 \cdot 5H_2O$ was added over a period of 1 h with continuous stirring under N_2 protection, and the color of the suspension changed from ochre to black. Stirring was then continued for an additional 30 min under N_2 at room temperature. The mixture was washed three times with methanol to remove excessive $NaBH_4$. Finally, the MMT/S-nZVI was freeze-dried and stored in an oxygen-free environment for use.

2.3 Material characterization

The morphological characteristics of MMT/S-nZVI were observed using a scanning electron microscope coupled with an energy-dispersive X-ray spectroscopy

(SEM-EDS, ZEISS GeminiSEM 300, Germany), during which elemental distribution analysis was conducted. All other materials were analyzed using SEM alone. Brunauer-Emmett-Teller (BET) surface area was determined by N_2 physical adsorption/desorption analysis on an ASAP 2460 (Micromeritics, USA). The surface charge of materials was measured using a zeta potential meter (BeNano 180 Zeta Pro, China). X-ray diffraction (XRD) analysis was performed using a MiniFlex600 diffractometer (Rigaku, Japan) with a Cu Kα radiation (40 kV/150 mA, λ=1.54056 Å). XRD data were collected in the scanning range of 3°-13° and 10°-80°, respectively. X-ray photoelectron spectroscopy (XPS) data were obtained on an AXIS-Ultra DLD instrument (Shimadzu, Japan) with Al Kα radiation (14.5 kV/15 mA). The scanning steps for the full and fractional spectra of XPS were 1 and 0.1 eV, respectively. Functional groups were characterized by Fourier-transform infrared spectroscopy (FTIR) on a Nicolet iS5 spectrometer (Thermo Fisher Scientificc, USA) with KBr pellet preparation, scanning from 4000 to 400 cm^{-1} at 4 cm^{-1} resolution and 8 scans.

2.4 Batch sorptive removal experiments

Batch experiments for the sorptive removal of Cd(II) and F-53B were conducted in 50.0 mL polypropylene centrifuge tubes containing 20.0 mL solution. Subsequently, 20.0 mg of materials (at a dosage of 1.0 g/L) were added to each tube. Based on the previous studies [27], the stock solution of Cd(II) and F-53B was then introduced into the system to achieve the final concentration of 50.0 mg/L Cd(II) and 1.0 mg/L F-53B, respectively. The initial pH of the solution was adjusted to 7.0 using 0.1 M HCl or NaOH as needed, unless otherwise specified for particular experiments. The sample tubes were placed on a model MQL-61R orbital shaker (Shanghai Minquan Instrument Co., Ltd, China) and shaken at 200 rpm at 25˚C throughout the experiment. Samples were collected at specified time intervals. All experimental procedures remained the same unless otherwise specified.

Sorption kinetics experiments were conducted using MMT, S-nZVI, Fe^{3+}-MMT, MMT/nZVI, and MMT/S-nZVI to investigate the removal efficiency for individual Cd(II) and F-53B. Sorption isotherm experiments were conducted to evaluate the

maximum sorption capacity of MMT/S-nZVI for individual Cd(II) and F-53B at various temperatures (25˚C, 35˚C and 45˚C), with initial Cd(II) concentrations of 0.0-200.0 mg/L and F-53B of 0.0-100.0 mg/L[28]. For the Cd(II)-F-53B co-contaminants, the effects of the initial concentrations of F-53B (0.0, 1.0 and 5.0 mg/L) and Cd(II) (0.0, 10.0 and 50.0 mg/L), MMT/S-nZVI dosages (0.1, 0.5, 1.0, 2.0, 3.0 g/L) and initial pH (3.0, 4.0, 5.0, 6.0, 7.0, 8.0 and 9.0) on the removal of Cd(II) and F-53B co-contaminants by MMT/S-nZVI were studied.

Furthermore, the removal performance of MMT/S-nZVI (0.1 g/L) was evaluated for Cd(II) (0.2 mg/L) and F-53B (0.001, 0.01 and 0.05 mg/L) co-contamination, as well as Cd(II) (0.2 mg/L) and a mixture of PFASs, at the environmentally relevant levels reported in the literature [9–11]. The PFASs mixture comprised 11 compounds and was carefully designed to represent the diverse PFAS profiles found in contaminated water[5,29,30]. Specifically, it included the legacy PFOS and its alternatives of F-53B, 6:2 fluorotelomer sulfonate (6:2 FTS), and short-chain perfluorobutanesulfonic acid (PFBS) and perfluorohexanesulfonic acid (PFHxS), legacy PFOA and its short-chain alternatives of perfluorobutanoic acid (PFBA), perfluorovaleric acid (PFPeA), perfluorohexanoic acid (PFHxA), perfluoroheptanoic acid (PFHpA), and the long-chain compound of perfluorodecanoic acid (PFDA), at the concentration of 0.001 mg/L each. All experiments were conducted in triplicate, and the average values with the error bars were reported. Prior to analysis, all sample supernatants were filtered through 0.02 μm hydrophilic syringe filters. For PFASs analysis, the filtered supernatants were diluted and subsequently centrifuged at 12,000 rpm for 15 min to remove potential matrix interferents before analysis. Other samples were analyzed directly after filtration.

2.5 Analytical methods

Cd(II) concentrations in solution were measured using a Hitachi Z-2000 atomic absorption spectrophotometer (AAS) with flame and graphite furnace methods, dual-beam optics (Zeeman effect), and direct current Zeeman background correction. F-53B concentrations in solution were analyzed by high-performance liquid

chromatography-tandem mass spectrometry (HPLC-MS/MS) using a Shimadzu LC-20A system coupled with an AB SCIEX API3200 mass spectrometer. The mass spectrometer operated in negative electrospray ionization (ESI) mode with multiple reaction monitoring (MRM). Chromatographic separation was achieved using an Agilent YMC-Triart C18 column (150.0 mm × 4.6 mm, 5.0 μm particle size) at 40°C. The mobile phase consisted of 10.0 mM ammonium acetate solution (A) and methanol (B), with a 10.0 μL injection volume, flowing at a rate of 0.8 mL/min. The limit of quantitation was 0.2 μg/L.

PFASs concentrations in solution were measured using a Waters (Milford, CT, USA) system composed of ACQUITY UPLC® H-Class quaternary pump, and XEVO TQ-S® triple-quadrupole mass spectrometer equipped with a Zspray® electrospray (ESI) interface in negative mode. Chromatographic separation was achieved using an ACQUTTY UPLC BEH C18 column (2.1 mm × 100.0 mm, 1.7 μm particle size) at 40°C. The mobile phase consisted of 5.0 mM ammonium acetate solution (A) and methanol (B), with a 2.0 μL injection volume, flowing at a rate of 0.3 mL/min. The limit of quantitation was 0.05-0.1 μg/L. The detailed MS/MS parameters for PFASs are provided in Table S1.

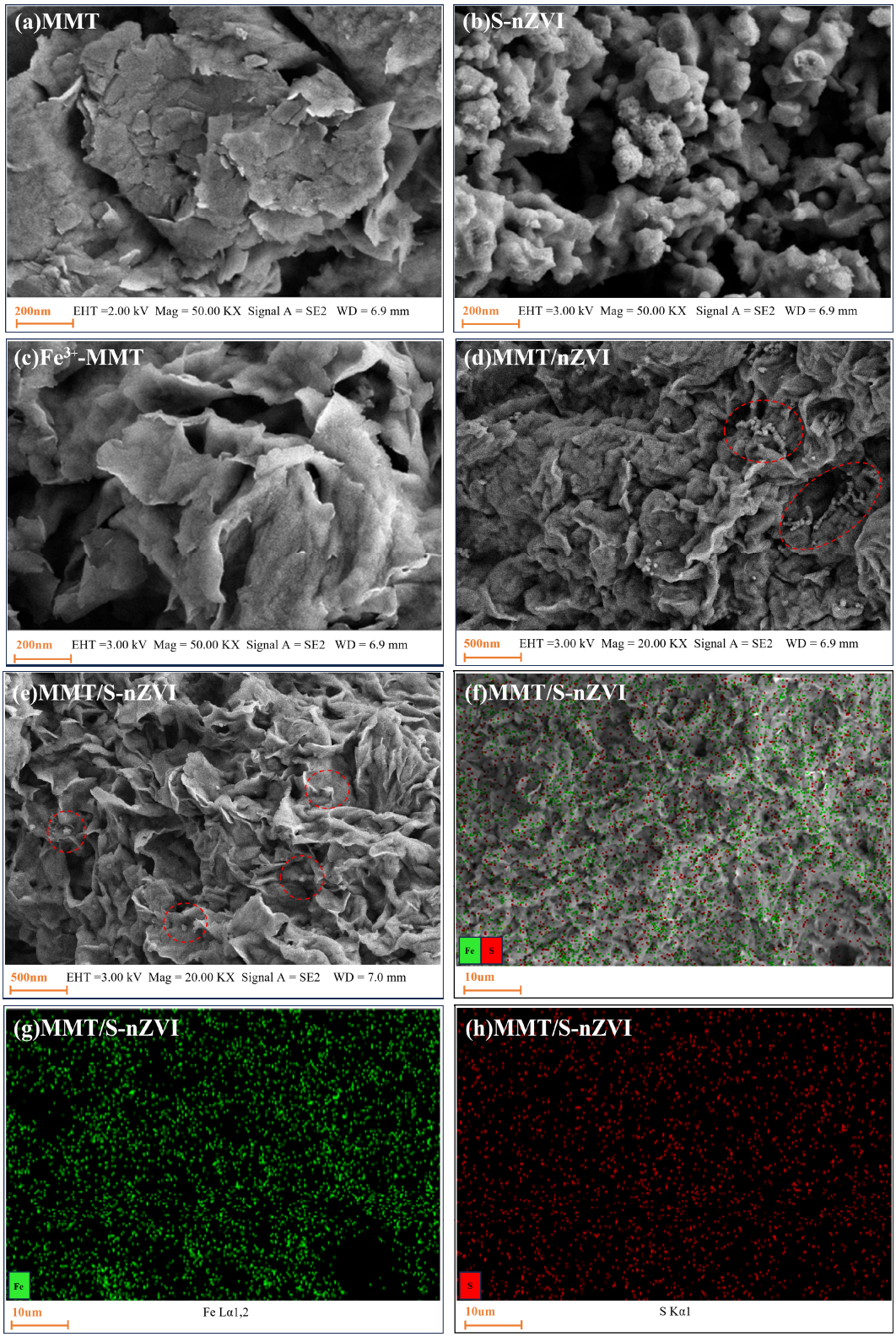
To determine the concentration of Fe ions in the solution after the sorptive removal of Cd(II) and F-53B by MMT/S-nZVI, 2.0 mL of the supernatant was collected, which was then filtered using a 0.02 μm hydrophilic syringe filter. The concentration of Fe ions was measured by atomic absorption spectroscopy (Z-2000, Hitachi Limited, Japan). The methods for calculating sorption kinetics and isotherms of Cd(II) and F-53B by the materials are detailed in Supporting Information (Text S1).

3 Results and discussion

3.1 Morphology and structural characterization

The morphologies of S-nZVI, MMT, Fe^{3+}-MMT, MMT/nZVI and MMT/S-nZVI investigated using SEM are presented in Figure 1. Both MMT and Fe^{3+}-MMT showed a layered structure (Figure 1a and 1c), suggesting that the crystal structure of MMT

was not altered by Fe^{3+}. On the other hand, chain-like aggregation of spherical particles was observed in the SEM image of S-nZVI (Figure 1b). Nano-spherical particles were clearly observed between the MMT layers of MMT/nZVI (Figure 1d), indicating the successful loading of nZVI onto MMT. The comparison of MMT/nZVI with MMT/S-nZVI (Figure 1d vs. Figure 1e) reveals that no significant aggregation of spherical particles was observed in MMT/S-nZVI after sulfidation, indicating that the aggregation phenomenon was alleviated by the sulfide modification [31]. The SEM-EDS images of MMT/S-nZVI (Figure 1f) revealed that Fe and S elements were uniformly distributed on the MMT surface, which further confirmed the successful loading of S-nZVI and its excellent dispersion. This uniform dispersion provides more accessible sorption sites for contaminant removal.



263

264 Figure 1 Morphology of (a) MMT, (b) S-nZVI, (c) Fe^{3+}-MMT, (d) MMT/nZVI, (e)

265 MMT/S-nZVI obtained from SEM, and (f-h) EDS diagrams of MMT/S-nZVI.

266

The zeta potential profiles within the pH range of 3.0-11.0 for the 5 prepared materials are presented in Figure 2a. All materials (except S-nZVI at low pH) displayed negative surface charges across the pH range investigated, with the absolute zeta potential increasing as pH increased. In addition, the absolute value of zeta potential of MMT/S-nZVI was higher than those of the other materials, indicating that it is less prone to aggregation and has better stability in aqueous solution [32], which is favorable for the sorption of contaminations.

Figure 2b displays the nitrogen adsorption–desorption isotherms of five materials. All MMT-based materials exhibited type IV isotherms with H_3 hysteresis loops, characteristic of layered structures [33], confirming that the structure of MMT remains intact after modification. Specific surface area data (Table S2) revealed no significant difference between Fe^{3+}-MMT and MMT, while MMT/nZVI and MMT/S-nZVI showed markedly lower values, likely due to nZVI induced clay particle aggregation and micropore blockage [34]. MMT/S-nZVI exhibited a larger specific surface area than MMT/nZVI, as SEM analysis revealed that sulfidation reduced nZVI aggregation, enabling more efficient nitrogen diffusion through MMT pores. In addition, MMT/S-nZVI and MMT/nZVI showed macro-mesoporous structures, unlike the micro-mesoporous structures of MMT and Fe^{3+}-MMT (Figure S1 and Table S2). Larger pores are known to enhance sorption through improved mass transport and increased active site availability [35].

XRD patterns within the angular 2θ ranges of 3°-12° and 10°-80° were studied. Figure 2c shows that the basal spacing decreased from 12.17 Å in pristine MMT to 11.12-11.68 Å after modification, consistent with previous reports of MMT layer contraction [36]. Additionally, the basal spacing of MMT/S-nZVI decreased slightly compared to MMT/nZVI, likely due to sulfidation improving nZVI dispersion and reducing interlayer aggregation. As shown in Figure 2d, the peaks observed at 20.1°, 35.4°, 54.3°, and 62.0° were attributed to MMT, whereas those located at 21.1° and 26.7° correspond to SiO_2 (PDF#85-0795) [19,22,37]. The patterns indicated that the crystal structure of MMT was not altered by loading of sulfonated nZVI [38].

Additionally, a peak at 44.5° was detected in the XRD spectrum of S-nZVI, MMT/nZVI and MMT/S-nZVI, which confirmed that Fe^0 (PDF#85-1410) was successfully loaded onto MMT [20]. However, no FeS were identified on S-nZVI and MMT/S-nZVI, possibly due to low degree of crystallinity of FeS or the overlapping with the peak of Fe^0 [39,40].

The chemical states of S and Fe on MMT/S-nZVI were further identified by XPS. The Fe 2p and S 2p spectra are shown in Figure 2e and 2f, respectively. The peak at 707.3 eV was attributed to Fe(0) or Fe(II)-S, and the peaks located at 713.9 eV and 712.0 eV correspond to Fe(III)-S and Fe(III)-O, respectively [41]. Various sulfur species were observed on the particles, including polysulfide (S_n^{2-}, 163.3 eV), disulfide (S_2^{2-}, 162.4 eV), and monosulfide (S^{2-}, 161.6 eV) [19]. The XPS results indicated that the surface of MMT/S-nZVI mainly contains Fe(0), FeS, FeS_2, FeS_n and other forms of iron-sulfur species, confirming the successful sulfurization of MMT/S-nZVI.

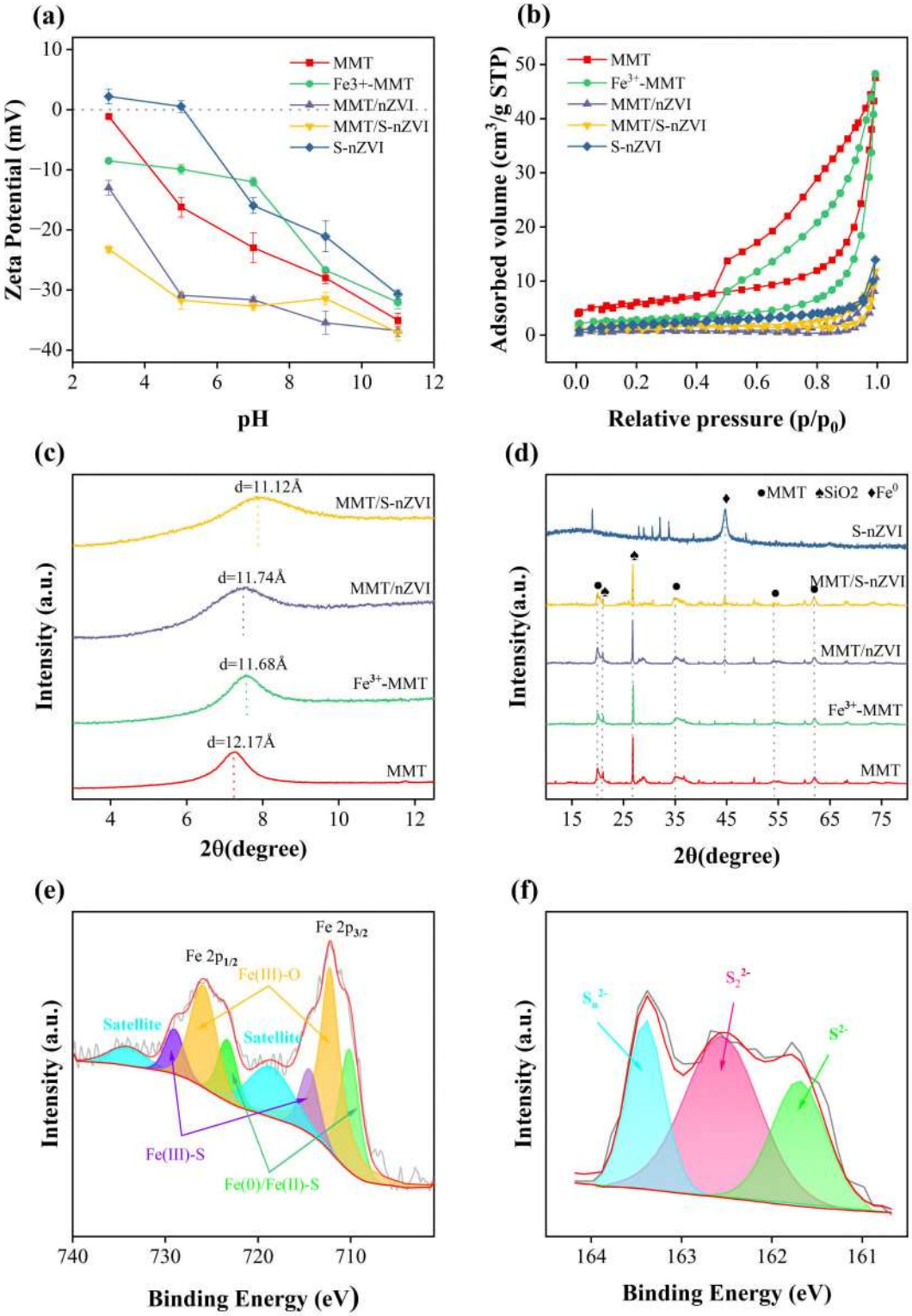


Figure. 2 (a) Zeta potential of materials; (b) N_2 adsorption-desorption isotherms of materials; XRD patterns of materials within 2θ range of (c) 3°-12° and (d) 10°-80°; (e) Fe 2p and (f) S 2p XPS spectrum of MMT/S-nZVI.

3.2 Sorption kinetics and isotherms of individual Cd(II) and F-53B by MMT/S-nZVI

3.2.1 Sorption kinetics of individual Cd(II) and F-53B

Sorption kinetics were investigated to compare the removal performance of five materials (MMT, S-nZVI, Fe^{3+}-MMT, MMT/nZVI, and MMT/S-nZVI) for the individual Cd(II) and F-53B (Figure 3). As shown in Figure 3a, the removal efficiency of Cd(II) by MMT/S-nZVI reached over 98.7% within 10 min, followed by S-nZVI (88.0%), MMT/nZVI (60.1%) and MMT (42.0%) within 30 min. The loading of S-nZVI onto MMT significantly improved Cd(II) removal. A similar trend was observed for kaolinite modified with S-nZVI, where the removal efficiency dramatically increased from 4.6% for pristine kaolinite to 93.2% for the S-nZVI@Kaol composite [20]. However, no significant sorptive removal of Cd(II) was observed for Fe^{3+}-MMT. The possible reasons include: (i) Fe^{3+} was adsorbed on the MMT surface, and it was difficult for Cd(II) to reach the MMT surface due to electrostatic interactions [23], resulting in no removal effect; (ii) trivalent iron ions are more readily adsorbed by MMT compared to divalent Cd ions [42]. As shown in Figure 3c, the removal efficiency of these materials for F-53B was comparable to their performance in Cd(II) removal. MMT/S-nZVI exhibited the highest F-53B removal efficiency, achieving 92.6% within 10 min, followed by Fe^{3+}-MMT (85.0% within 10 min), S-nZVI (65.1% within 30 min), MMT/nZVI (58.4% within 60 min), and MMT (24.3% within 60 min). At the same initial F-53B concentration of 1.0 mg/L, the performance of MMT/S-nZVI is comparable to that of modified biochar, which achieves over 95% removal [43]. As shown in Figure S2, the hydrophobicity of MMT/S-nZVI was increased compared to MMT, which is attributed to the introduction of highly hydrophobic S-nZVI with surface iron sulfide compounds [44]. This increased hydrophobicity substantially improved F-53B sorption by MMT/S-nZVI. The higher removal efficiency of F-53B by Fe^{3+}-MMT compared to MMT may be due to the sorption of Fe^{3+} onto the MMT surface through cation exchange, which activates surface hydroxyl groups that form complexes with F-53B

ions [45].

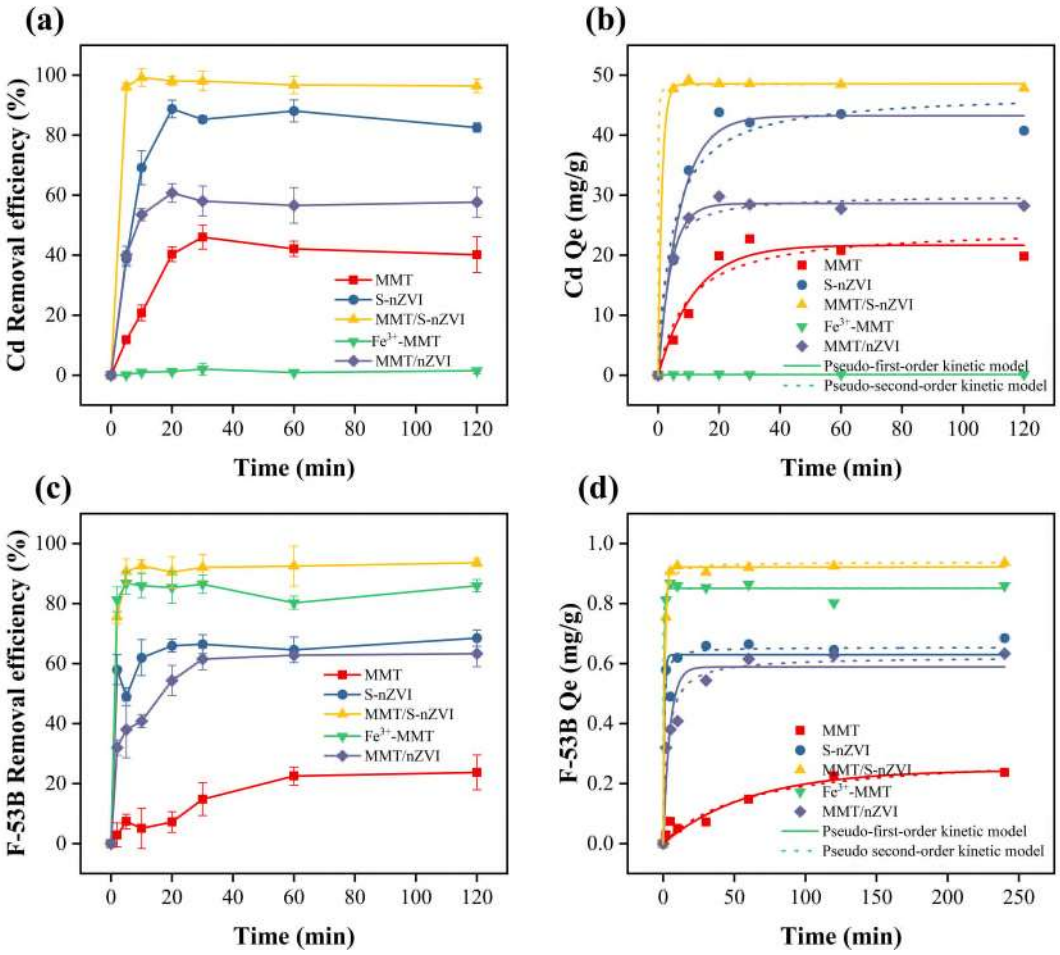


Figure. 3 Removal efficiency of individual (a) Cd(II) and (c) F-53B, and sorption kinetics of individual (b) Cd(II) and (d) F-53B by different materials. The initial concentrations of Cd(II) and F-53B were 50.0 mg/L and 1.0 mg/L, respectively.

The sorption kinetics fittings of individual Cd(II) and F-53B by different materials are shown in Figure 3b and 3d, respectively, and the fitting parameters are summarized in Table S3. It was observed that the sorptive removal of Cd(II) by MMT and Fe^{3+}-MMT fit the pseudo-first-order kinetic model, indicating primarily through physical sorption. In contrast, S-nZVI, MMT/nZVI, and MMT/S-nZVI fit the pseudo-second-order kinetic model more closely, suggesting dominant chemical sorption due to the presence of nZVI. For the removal of F-53B by all five materials, the fittings align more closely with the pseudo-second-order kinetic model. In addition, as indicated by the kinetics fitting parameters in Table S3, the removal rates and equilibrium sorption capacities of MMT/S-nZVI for both Cd(II) and F-53B were significantly higher than

those of other materials. This indicated that the MMT loaded with S-nZVI facilitates the removal of both Cd(II) and F-53B.

3.2.2 Sorption isotherms of individual Cd(II) and F-53B by MMT/S-nZVI

The sorption isotherms of individual Cd(II) and F-53B by MMT/S-nZVI at 25˚C, 35˚C and 45˚C are shown in Figure 4, and the fitting parameters using both the Langmuir and Freundlich models are presented in Table S4. The results indicated that the Langmuir model (R^2 = 0.69-0.95) better described the sorption process of Cd(II) at different temperatures, suggesting that the sorptive removal of Cd(II) was mainly monolayer sorption [46]. In contrast, both the Langmuir (R^2 = 0.95-0.97) and Freundlich models (R^2 = 0.98-0.99) provided good fits for the sorption process of F-53B, indicating the sorption process of F-53B on MMT/S-nZVI is more complex and involves both monolayer and multilayer sorption mechanisms [37,46]. Based on the values of Q_{max} and b in Table S4, both the maximum sorption capacity and intensity for Cd(II) and F-53B increased gradually with increasing temperatures. When the temperature increased from 25 to 45°C, the maximum sorption capacity of MMT/S-nZVI increased from 157.5 to 171.4 mg/g for Cd(II), while that for F-53B increased from 22.3 to 23.6 mg/g. These results demonstrated that the sorptive removal of Cd(II) and F-53B by MMT/S-nZVI was an endothermic process. Similar studies have reported an increase in the adsorption capacity for Cd(II) using S-nZVI and F-53B by four kinds of nano-materials[26,46]. Theoretically, a temperature increase raises the entropy of the system, thereby enhancing the probability of effective contacts conducive to sorption. In addition, temperature influences particle aggregation by affecting random Brownian motion and collision frequency, which subsequently exerts a notable impact on the sorption process [46]. The Freundlich constant (*n*) value for Cd(II) and F-53B was greater than 1, indicating favorable sorption of Cd(II) and F-53B on MMT/S-nZVI [47].

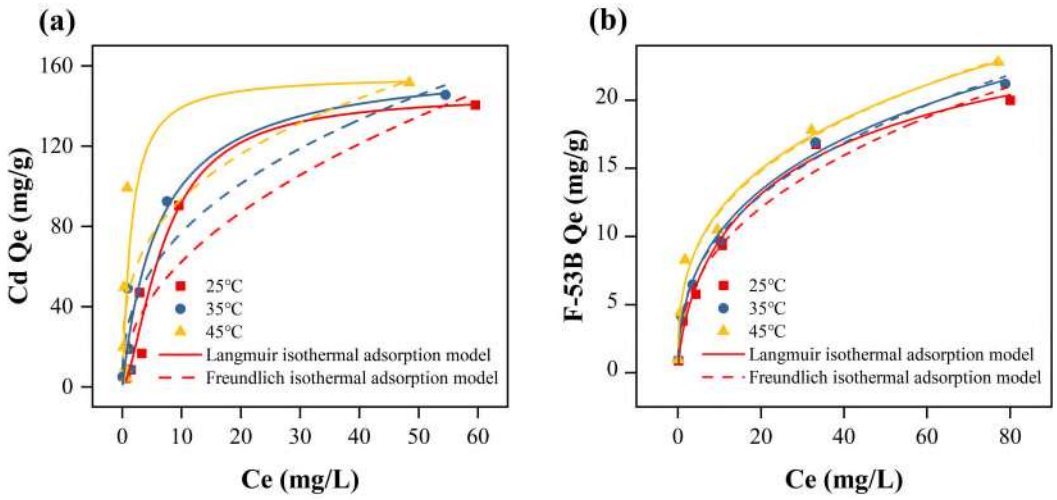


Figure. 4 Sorption isotherms of individual (a) Cd(II) and (b) F-53B by MMT/S-nZVI at 25, 35 and 45°C.

3.3 Removal of Cd(II) and F-53B co-contaminants by MMT/S-nZVI under various influencing factors

The influence of initial concentration on the removal efficiency of Cd(II) and F-53B co-contamination by MMT/S-nZVI is shown in Figure 5a and 5b, respectively. Under co-contamination conditions, the removal efficiency of Cd(II) by MMT/S-nZVI was 94.0% at 5.0 mg/L F-53B, slightly lower than that (98.7%) under individual contamination (Figure. 5a). These results indicated that the presence of F-53B had little effect on Cd(II) removal. In contrast, the presence of Cd(II) reduced F-53B removal efficiency from 89.6% (individual) to 69.0% when the Cd(II) concentration increased to 50.0 mg/L (Figure. 5b). It was reported that Cd(II) could react with the $Fe(OH)_2$ and FeS to form $Cd(OH)_2$ and CdS precipitates and some complexes [26,32]. Therefore, the reaction between Cd(II) and FeS on MMT/S-nZVI reduces the amount of available FeS, and the generated precipitates and complexes may cover the surface of S-nZVI, thereby blocking active sites and reducing the hydrophobic sorption capacity of MMT/S-nZVI. Consequently, the presence of Cd(II) leads to a decrease in the removal of F-53B. Moreover, due to the electrostatic attraction between the cations and anions, it is speculated that electrostatic sorption also exists between Cd(II) and F-53B [48], which leads to a decrease in the sorption of Cd(II) and F-53B on MMT/S-nZVI.

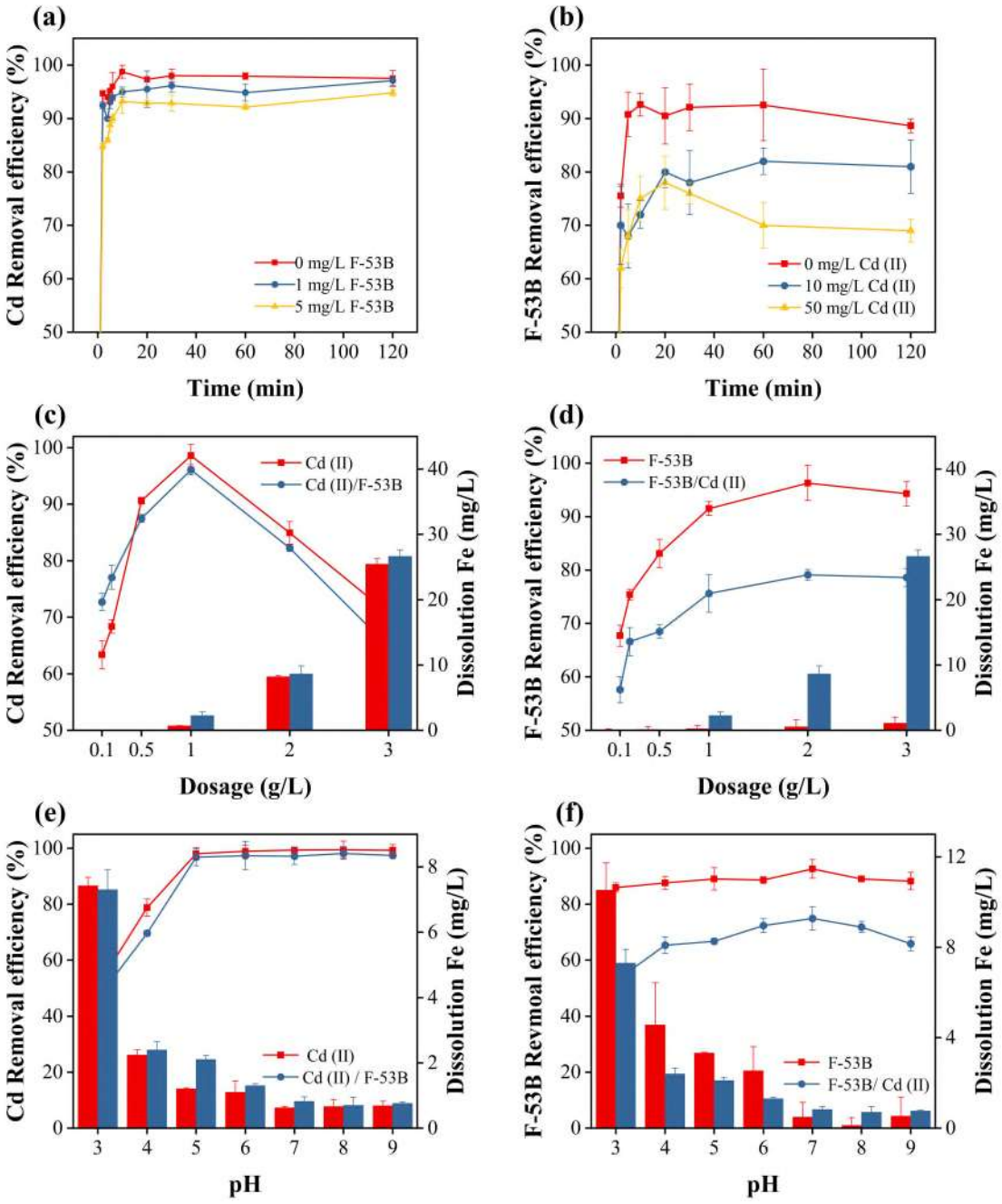


Figure. 5 Effects of experimental parameters on the removal of Cd(II) and F-53B by MMT/S-nZVI: (a, b) influence of initial contaminant concentrations; (c, d) effect of MMT/S-nZVI dosage on removal efficiency and Fe ion concentration; (e, f) impact of initial solution pH on removal efficiency and Fe ion release. Removal efficiencies are shown as line graphs, and Fe ion concentrations as bar graphs. Initial concentrations of Cd(II) and F-53B were 50.0 mg/L and 1.0 mg/L, respectively..

The removal of Cd(II) and F-53B co-contamination under different doses of MMT/S-nZVI is presented in Figure 5c and 5d. The results in Figure 5c indicated that for both individual Cd(II) and co-contamination conditions, the removal efficiency of Cd(II) increased with increasing dosage of MMT/S-nZVI, and reaching the highest of 98.7% and 95.0% under individual and co-contamination at 1.0 g/L, respectively, then declined beyond 1.0 g/L. In addition, as the dosage increased, the Fe ions concentration increased rapidly, reaching 25.0 mg/L and 26.0 mg/L at 3.0 g/L in the individual and co-contamination systems, respectively. It has been shown that Cd(II) promoted the hydrolysis of Fe^0 to produce more iron ions and depassivate Fe^0 [49,50]. Therefore, as the dosage of MMT/S-nZVI increased, the enhanced Fe content amplifies the Cd(II) promoted dissolution of Fe ions, resulting in a significant increase in the concentration of Fe ions in solution. However, MMT's strong cation exchange capacity leads to competition between Fe ions and Cd(II) for sorption sites, thereby reduced the sorptive removal efficiency of Cd(II) by MMT/S-nZVI.

Figure 5d illustrates that F-53B removal efficiency increased with increasing dosage of MMT/S-nZVI and finally stabilized under individual and co-contamination conditions. However, the overall removal efficiency of individual F-53B contamination was higher than that of co-contamination. At a dosage of 1.0 g/L, F-53B removal efficiency was 91.0% and 75.0% under individual and co-contamination, respectively, while the highest removal was achieved at a dosage of 2.0 g/L, which was 95.0% and 78.0%, respectively. In the case of individual F-53B contamination, the concentration of Fe ions in solution was low and increased slightly with the increase in dosage. However, in the presence of Cd(II), the concentration of Fe ions increased rapidly. This further indicated that Cd(II) would promote the dissolution of Fe ions. Under individual F-53B and co-contamination conditions at a dosage of 3.0 g/L, the highest concentrations of Fe ions were 3.0 mg/L and 27.0 mg/L, respectively. At these points, 93.0% and 77.5% of F-53B were removed. These values showed no significant decrease compared to the highest removal efficiencies observed (95.0% and 78.0%), indicating that the concentration of Fe ions has little impact on

the removal of F-53B.

Solution pH critically influenced sorption by altering the ionization state of surface groups, as confirmed by zeta potential measurements (Section 3.1). Therefore, the removal efficiency of Cd(II) and F-53B co-contamination by MMT/S-nZVI under different pH was investigated (Figure 5e and 5f). As shown in Figure 5e, the removal of Cd(II) by MMT/S-nZVI, both in the presence and absence of F-53B, increased from about 40.0% to 95.0% with the initial pH increased from 3 to 5. When pH was exceeded 5, no significant change in the removal of Cd(II) was observed. Additionally, the concentration of Fe ions in the solution gradually decreased as the pH increased. It has been reported that under acidic conditions, FeS undergoes proton-facilitated dissolution, resulting in the release of dissolved ferrous ions [51]. Figure 2a demonstrated that as pH increased, the amount of negative charges on the MMT/S-nZVI surface increased, thereby enhancing the electrostatic attraction between MMT/S-nZVI and Cd(II). Under strongly acidic conditions, the electrostatic sorption of Cd(II) by MMT/S-nZVI was inhibited due to the competitive effects of H^+ and Fe ions, further reducing the removal efficiency of Cd(II) by MMT/S-nZVI. However, when the initial pH increased, the presence of OH^- ions enhanced the electrostatic attraction between Cd(II) and MMT/S-nZVI [49], thereby improving the removal efficiency of Cd(II). For F-53B (Figure 5f), the removal efficiency followed a similar trend across pH values under both individual contamination and co-contamination with Cd(II). The removal ranged from 86.0% to 91.5% in individual systems and from 50.0% to 75.0% in co-contaminated systems. These results indicated that pH had no significant influence on F-53B removal. Nevertheless, the slight decrease for F-53B removal observed specifically at pH 7-9 in the co-contamination system is likely due to competitive sorption, where Cd(II) ions occupy the active sites on the MMT/S-nZVI surface, thereby inhibiting the sorption of F-53B. Furthermore, the presence of Cd(II) was observed to inhibite the dissolution of Fe ions compared to the individual F-53B system at pH 3-6. Under acidic conditions, the F-53B-only system continuously releases Fe^{2+} due to the proton-driven dissolution

of FeS ($FeS + 2H^+ \rightarrow Fe^{2+} + H_2S$) [26]. In the Cd(II) co-contamination system, although the ion exchange process initially releases some iron, the newly formed CdS precipitates deposit on the S-nZVI surface and form a protective layer that effectively blocks further proton attack. This inhibits long-term corrosion and iron release, resulting in lower net iron leaching than in the F-53B-only system. Generally, under neutral to alkaline conditions (pH 7-9), 1 g/L of MMT/S-nZVI demonstrated high efficiency in the simultaneous removal of Cd(II) and F-53B from co-contaminated systems, with minimal Fe leaching (< 2.0 mg/L). Given that iron is a common groundwater mineral and its concentration complies with China's Class IV groundwater standard (GB/T 14848-2017, ≤ 2.0 mg/L), the risk of secondary pollution under these conditions is considered minimal. However, a comprehensive assessment of the material's long-term stability is essential for its practical application and should be a key focus of future research. For practical implementation, it is recommended to adjust the water pH to this range as necessary to ensure optimal performance and long-term stability.

3.4 Removal of Cd(II) and the mixture of PFAS compounds by MMT/S-nZVI at environmentally relevant levels

Figure 6 shows the removal efficiency of Cd(II) and F-53B, Cd(II) and the mixture of 11 multiple PFAS compounds by MMT/S-nZVI at environmentally relevant levels. The results revealed that in the presence of co-contaminants, the removal efficiency of Cd(II) was maintained at ~ 98.0% with the initial F-53B concentrations at 0.001, 0.01 and 0.05 mg/L. The removal efficiency of F-53B exhibited a concentration-dependent increase, from 13.0% at 0.001 mg/L to 36.5% at 0.05 mg/L, in the presence of 0.2 mg/L Cd(II) (Figure 6a). It is hypothesized that the higher the concentration, the higher the frequency of contact between MMT/S-nZVI and F-53B, the higher the possibility of sorption.

Figure 6b showed that the removal efficiency of Cd(II) was 98.9% by MMT/S-nZVI in the presence of a mixture of 11 PFASs, while the removal efficiencies for the various PFASs ranged from 0.0% to 20.0%. The results revealed that the longer-chain

compounds, i.e., PFDA, PFOA, PFHpA among perfluorocarboxylic acids (PFCAs) and F-53B, 6:2 FTS and PFOS among perfluorosulfuric acids (PFSAs), had higher removal efficiencies than those with shorter-chain, consistent with the conclusions from previous publications [52]. The long-chain PFASs preferentially adsorb onto MMT/S-nZVI due to their stronger hydrophobic interactions [53]. It was also worth noting that no removal of PFBA, PFPeA, PFH_XA was observed, and the removal of PFBS and PFH_XS were 4.0% and 6.0%, respectively, suggesting that the removal of short-chain PFAS compounds more challenging than those with long-chain by MMT/S-nZVI. The limited removal of short-chain PFASs is a widely reported challenge for a broad range of adsorbents[54,55]. To address this issue, a fundamental understanding of the removal mechanisms and key environmental factors is essential to guide the development of optimized strategies. Furthermore, research is increasingly focused on the rational design of advanced functional materials with enhanced affinity for short-chain PFASs [55,56].

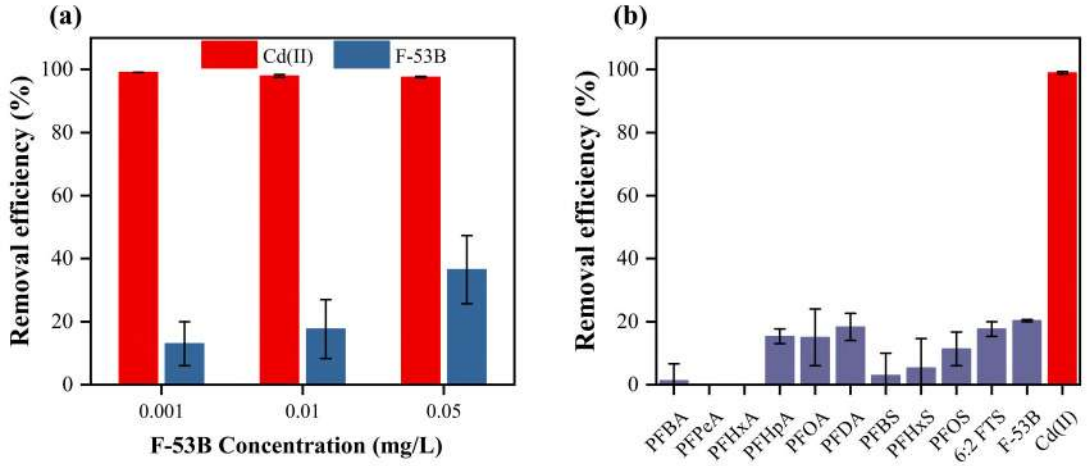


Figure. 6 Removal efficiency of Cd(II) and F-53B co-contamination (a), Cd(II) and the mixture of 11 PFASs (b) by MMT/S-nZVI at environmentally relevant levels. The concentrations were 0.2 mg/L for Cd(II) and 0.001 mg/L for each PFAS compound.

The results demonstrated that MMT/S-nZVI exhibited excellent removal performance for Cd(II) removal and was capable of simultaneously removing multiple PFASs at environmentally relevant levels, which was of importance for practical applications. It was indicated that Cd(II) removal efficiency was not affected significantly by the

presence of F-53B or the mixture of PFAS compounds. Moreover, the PFAS mixture also had negligible on F-53B removal. The removal of various PFASs was influenced by their own carbon-chain lengths [53]and it was more challenging to remove the short-chain PFAS compounds from water solutions.

3.5 Removal mechanisms of Cd(II) and F-53B co-contamination by MMT/S-nZVI

The characterization of MMT/S-nZVI before and after sorption with Cd(II) and F-53B, as shown in Figure 7, provides valuable insights into the removal mechanisms for the co-contaminants (Figure 8). The FTIR analysis of MMT/S-nZVI in Figure 7a and Table S5, revealed that significant functional groups inherent to MMT, including hydroxyl groups present on the MMT layers, interlayer water molecules, and Si-O and Al-O bonds [57], provide MMT/S-nZVI with the necessary framework for effective sorptive interactions. After exposure to F-53B, either individually or in a co-contaminated system, the FTIR spectra showed notable stretching vibration peaks for S=O and C-F bonds within the absorption bands of 1400–1050 cm^{-1} [58,59], indicative of the successful sorption of F-53B onto the MMT/S-nZVI composite. The appearance of new characteristic peaks at 293.3 eV (K 2p) and 688.4 eV (F 1s) after sorption further confirmed the successful sorption of F-53B onto the MMT/S-nZVI surface (Figure 7b). These peaks were consistent with the presence of the fluorinated functional groups in F-53B. The new peak observed at 405.4 eV corresponds to the Cd element [16], further validating the immobilization of Cd(II) on the MMT/S-nZVI. The Cd $3d_{3/2}$ and Cd $3d_{5/2}$ spectra (Figure S3) indicated no changes in the valence state of Cd(II) during sorption, suggesting that Cd(II) was not reduced or oxidized during the interaction with MMT/S-nZVI [16,60]. This points to sorption and co-precipitation as the primary immobilization mechanisms for Cd(II). These XPS findings provided direct evidence of the successful sorption of both Cd(II) and F-53B, and confirmed that MMT/S-nZVI effectively immobilized Cd(II) and adsorbed F-53B without altering the valence state of Cd(II). This highlights the material's suitability for addressing co-contamination scenarios.

The XRD analysis of MMT/S-nZVI (Figure 7c) revealed significant changes in the interlayer spacing after sorption of Cd(II), F-53B, and their co-contaminant. The basal spacing of MMT/S-nZVI increased from 11.12 Å (before sorption) to 12.61 Å, 11.93 Å, and 14.78 Å after sorption of Cd(II), F-53B, and their co-contaminants, respectively. The largest increase was observed after co-contaminant sorption, suggesting that both Cd(II) and F-53B penetrated the interlayers of MMT/S-nZVI. MMT's high cation exchange capacity facilitated the entry of Cd(II) into its interlayer, replacing existing cations in the interlayer through a cation exchange mechanism, as previously reported [61]. F-53B molecules were likely adsorbed into the interlayer by forming complexes with hydrated cations present in the interlayer. Electrostatic interactions between the negatively charged functional groups of F-53B and the interlayer cations played a crucial role in this process [62]. Despite the changes in interlayer spacing, the fundamental structure of MMT/S-nZVI remained intact. This demonstrated the material's robustness and adaptability for simultaneous sorption of different contaminants.

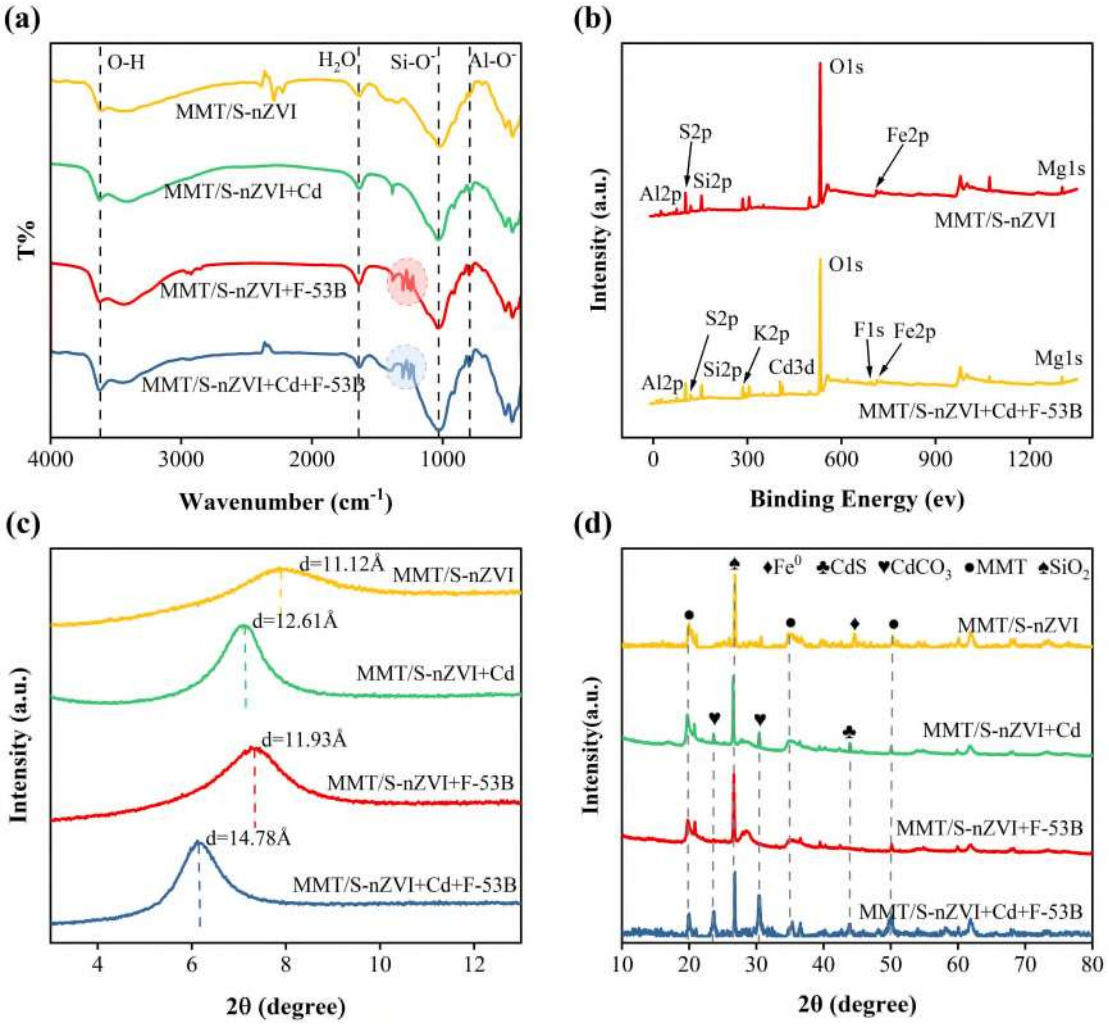


Figure. 7 Characterization of MMT/S-nZVI before and after reaction: (a) FTIR spectra; (b) XPS spectra of full spectrum scan; XRD spectra of 2θ range from (c) 3° to 12° and (d) 10° to 80°.

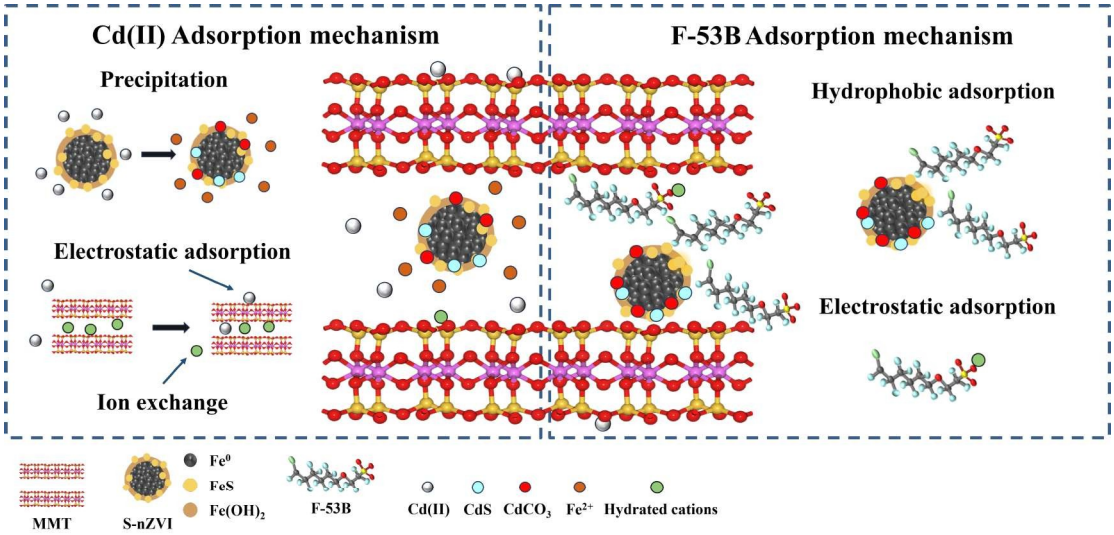
The analysis of XRD patterns in Figure 7d provided key insights into the mechanisms of Cd(II) removal by MMT/S-nZVI under both individual and co-contaminated conditions. All spectra exhibited a consistent peak at 26.6°, corresponding to SiO_2 (PDF#85-0795), alongside other characteristic peaks of MMT, indicating that the MMT structure remained largely unchanged before and after the sorption process, confirming the stability of the MMT framework. In addition, two new peaks at 2θ values of 23.5° and 30.3° were observed, consistent with the crystalline phase of $CdCO_3$ (PDF#42-1342). This suggested that $Cd(OH)_2$, initially formed via reactions with hydroxide ions, reacts further with CO_2 from the air to form $CdCO_3$ precipitates. A peak at 44.0° corresponding to CdS (PDF#10-0454) was also observed. This

aligned with the reaction of Cd(II) with sulfur present in the S-nZVI, forming CdS precipitates, as reported in the literature [63,64].

These findings demonstrated that the removal of Cd(II) by MMT/S-nZVI was facilitated by a combination of electrostatic adsorption, cation exchange, and precipitation processes. The Cd(II) was initially adsorbed onto the MMT/S-nZVI surface via electrostatic interactions, which was critical for initiating the removal process. In addition, Cd(II) ions can also exchange with cations in the interlayer of MMT, enhancing the retention of Cd(II) within the material. Furthermore, Cd(II) can react with hydroxide ions and sulfur species to generate $Cd(OH)_2$ and CdS precipitates. The formation of these precipitates highlights the critical role of both the MMT structure and S-nZVI in achieving efficient heavy metal remediation. The sorption of F-53B involved two primary interactions: hydrophobic interactions and electrostatic interactions. The hydrophobic nature of S-nZVI played a role in attracting F-53B to the surface and interlayers of the composite [44,65]. The hydrated cations within the interlayer of MMT can form complexes with the functional groups of F-53B, enhancing its sorption. These findings underscore the functional capabilities of MMT/S-nZVI in addressing environmental contaminants like F-53B, leveraging both physical and chemical interaction pathways.

Under co-contamination conditions, the removal efficiency of F-53B and Cd(II) by MMT/S-nZVI was reduced compared to their individual removal scenarios. This decrease was primarily attributed to several interrelated factors. The interaction between Cd(II) and S-nZVI led to the precipitates that accumulated on the surface of MMT/S-nZVI. This layer obstructs active sites, limiting the availability of FeS, which was crucial for effective sorption processes. Consequently, the hydrophobic interactions between MMT/S-nZVI and F-53B were diminished, impairing F-53B removal efficiency. In addition, electrostatic attractions exist between Cd(II), solubilized Fe ions, and F-53B. This reduced the availability of free contaminants for sorption, resulting in a simultaneous decline in the removal efficiencies of both F-53B and Cd(II). This interplay of surface passivation, and complex formation underscores

609 the challenges of addressing co-contaminated systems, highlighting the need for
610 tailored remediation strategies to mitigate such interference effects.



611
612 Figure. 8 Mechanisms of simultaneous removal of Cd(II) and F-53B
613 co-contamination by MMT/S-nZVI.

614 **4 Conclusions**

615 This study successfully synthesized a novel MMT/S-nZVI composite and
616 demonstrated its efficacy for the co-removal of Cd(II) and F-53B from aqueous
617 solutions. The high removal efficiency of the composite was due to the synergistic
618 combination of the superior adsorption and cation exchange capabilities of MMT with
619 the reactivity and hydrophobicity of S-nZVI. The elucidation of how Cd(II)
620 compromises F-53B adsorption by consuming sulfur sites and altering surface
621 hydrophobicity is an important finding to consider for real-world applications as
622 pollutants rarely exist in isolation. The composite's ability to simultaneously remove
623 Cd and multiple PFASs at environmentally relevant concentrations, demonstrates its
624 potential for field application in treating co-contaminated water, such as electroplating
625 wastewater. However, the reduced efficacy for short-chain PFASs confirms a
626 persistent challenge in the field. Overall, the implications of this work are twofold: (1)
627 it presents MMT/S-nZVI as a versatile and effective sorbent for complex pollution
628 scenarios, and (2) it offers a mechanistic framework that can guide the future design
629 of advanced multifunctional materials for the concurrent remediation of heavy metals

and persistent organic pollutants. Future efforts should focus on optimizing the material to mitigate competitive inhibition and enhance short-chain PFASs removal efficiency. In addition, it is recommended that the evaluation of its performance in real environmental waters and long-term stability over repeated use cycles, so as to provide a fundamental basis for its practical applications.

Supporting Information

Methods for calculating sorption kinetics and isotherms (Text S1); Optimized MRM conditions for PFASs detection using MS/MS (Table S1); BET surface area and pore structure parameters of different materials (Table S2); Pseudo-first and pseudo-second order kinetics fitting parameters for the sorptive removal of individual Cd(II) and F-53B by different materials (Table S3); Fitting parameters for isothermal sorption of individual Cd(II) and F-53B by MMT/S-nZVI at different temperatures (Table S4); FTIR wavenumbers and their assignments of MMT/S-nZVI (Table S5); Pore diameter distribution of MMT, Fe^{3+}-MMT, MMT/nZVI, S-nZVI and MMT/S-nZVI (Figure S1); Water contact angle of MMT and MMT/S-nZVI (Figure S2); Cd 3d XPS spectrum of MMT/S-nZVI after sorption with Cd(II) and F-53B (Figure S3)

Acknowledgment

This research was supported by grants from the National Natural Science Foundation of China (No. 32061133001), CSCEC Eco-Environmental Engineering Research Center (Soil Remediation Technology and Equipment) (No. CSCEC-PT-009), and Shandong Leading Green Industry Development Corporation (Green Industry and Environmental Safety Innovation and Entrepreneurship Community of Shandong Province) (No. 2023-LSGTT-CX-004). We acknowledge the cooperation between China and the EU through the EiCLaR project (European Union's Horizon 2020, N°965945).

Author Contributions

CRediT: **Qing Wang**: Writing – original draft, Writing – review & editing, Validation, Conceptualization; **Yi Zhou**: Writing – original draft, Investigation, Visualization;

Liangchun Jia: Methodology, Investigation, Data Curation; **Frederic Coulon** Writing – review & editing; **Changxun Dong**: Writing – review & editing; **Bo Zhang**: Supervision, Writing – review & editing; **Guangwen Zhu**: Validation; **Xin Song**: Writing – review & editing, Supervision, Conceptualization, Funding acquisition.

References

(1) Zhang, W.; Li, J.; Huang, R.; Zhang, X.; Wang, Y.; Zhou, D.; Xian, Q. Effect of Coexisting Cd(II) and as(V) on Anionic PFASs Sorption in Soils: Models and Mechanisms. *Environ. Pollut.* **2025**, *370*, 125917. https://doi.org/10.1016/j.envpol.2025.125917.

(2) Xiao, D.; Dong, W.; Wang, H.; Cao, J.; Liu, J.; Wang, Y.; Wu, Y.; Ma, F.; Yi, H. Drosera-Inspired Zirconium-Based Coagulant for Simultaneous Removal of F^-, PFAS and Heavy Metals from Wastewater. *Chem. Eng. J.* **2025**, *519*, 164887. https://doi.org/10.1016/j.cej.2025.164887.

(3) Saikat, S.; Kreis, I.; Davies, B.; Bridgman, S.; Kamanyire, R. The Impact of PFOS on Health in the General Population: A Review. *Env. Sci Process. Impacts* **2013**, *15* (2), 329–335. https://doi.org/10.1039/C2EM30698K.

(4) Gebbink, W. A.; Bossi, R.; Rigét, F. F.; Rosing-Asvid, A.; Sonne, C.; Dietz, R. Observation of Emerging Per- and Polyfluoroalkyl Substances (PFASs) in Greenland Marine Mammals. *Chemosphere* **2016**, *144*, 2384–2391. https://doi.org/10.1016/j.chemosphere.2015.10.116.

(5) Hamid, N.; Junaid, M.; Sultan, M.; Yoganandham, S. T.; Chuan, O. M. The Untold Story of PFAS Alternatives: Insights into the Occurrence, Ecotoxicological Impacts, and Removal Strategies in the Aquatic Environment. *Water Res.* **2024**, *250*, 121044. https://doi.org/10.1016/j.watres.2023.121044.

(6) Munoz, G.; Liu, J.; Duy, S. V.; Sauvé, S. Analysis of F-53B, Gen-X, ADONA, and Emerging Fluoroalkylether Substances in Environmental and Biomonitoring Samples: A Review. *Trends Environ. Anal. Chem.* **2019**, *23*, e00066. https://doi.org/10.1016/j.teac.2019.e00066.

(7) Pan, Y.; Zhang, H.; Cui, Q.; Sheng, N.; Yeung, L. W. Y.; Sun, Y.; Guo, Y.; Dai, J. Worldwide Distribution of Novel Perfluoroether Carboxylic and Sulfonic Acids in Surface Water. *Environ. Sci. Technol.* **2018**, *52* (14), 7621–7629. https://doi.org/10.1021/acs.est.8b00829.

(8) Wang, S.; Huang, J.; Yang, Y.; Hui, Y.; Ge, Y.; Larssen, T.; Yu, G.; Deng, S.; Wang, B.; Harman, C. First Report of a Chinese PFOS Alternative Overlooked for 30 Years: Its Toxicity, Persistence, and Presence in the Environment. *Environ. Sci. Technol.* **2013**, *47* (18), 10163–10170. https://doi.org/10.1021/es401525n.

(9) Liu, S.; Jin, B.; Arp, H. P. H.; Chen, W.; Liu, Y.; Zhang, G. The Fate and Transport of Chlorinated Polyfluorinated Ether Sulfonates and Other PFAS through Industrial Wastewater Treatment Facilities in China. *Environ. Sci. Technol.* **2022**, *56* (5), 3002–3010. https://doi.org/10.1021/acs.est.1c04276.

(10) Kumar, V.; Parihar, R. D.; Sharma, A.; Bakshi, P.; Sidhu, G. P. S.; Bali, A. S.; Karaouzas, I.; Bhardwaj, R.; Thukral, A. K.; Gyasi-Agyei, Y.; Rodrigo-Comino, J. Global Evaluation of Heavy Metal Content in Surface Water Bodies: A Meta-Analysis Using Heavy Metal Pollution Indices and Multivariate Statistical Analyses. *Chemosphere* **2019**, *236*, 124364.

https://doi.org/10.1016/j.chemosphere.2019.124364.
(11) Monika Mahajan; Gupta, P. K.; Singh, A.; Vaish, B.; Singh, P.; Kothari, R.; Singh, R. P. A Comprehensive Study on Aquatic Chemistry, Health Risk and Remediation Techniques of Cadmium in Groundwater. *Sci. Total Environ.* **2022**, *818*, 151784. https://doi.org/10.1016/j.scitotenv.2021.151784.
(12) Zhang, D. Q.; Zhang, W. L.; Liang, Y. N. Adsorption of Perfluoroalkyl and Polyfluoroalkyl Substances (PFASs) from Aqueous Solution - a Review. *Sci. Total Environ.* **2019**, *694*, 133606. https://doi.org/10.1016/j.scitotenv.2019.133606.
(13) Chai, W. S.; Cheun, J. Y.; Kumar, P. S.; Mubashir, M.; Majeed, Z.; Banat, F.; Ho, S.-H.; Show, P. L. A Review on Conventional and Novel Materials towards Heavy Metal Adsorption in Wastewater Treatment Application. *J. Clean. Prod.* **2021**, *296*, 126589. https://doi.org/10.1016/j.jclepro.2021.126589.
(14) Xu, B.; Liu, S.; Zhou, J. L.; Zheng, C.; Weifeng, J.; Chen, B.; Zhang, T.; Qiu, W. PFAS and Their Substitutes in Groundwater: Occurrence, Transformation and Remediation. *J. Hazard. Mater.* **2021**, *412*, 125159. https://doi.org/10.1016/j.jhazmat.2021.125159.
(15) Zhou, L.; Li, Z.; Yi, Y.; Tsang, E. P.; Fang, Z. Increasing the Electron Selectivity of Nanoscale Zero-Valent Iron in Environmental Remediation: A Review. *J. Hazard. Mater.* **2022**, *421*, 126709. https://doi.org/10.1016/j.jhazmat.2021.126709.
(16) Zhang, Y.; Li, Y.; Dai, C.; Zhou, X.; Zhang, W. Sequestration of Cd(II) with Nanoscale Zero-Valent Iron (nZVI): Characterization and Test in a Two-Stage System. *Chem. Eng. J.* **2014**, *244*, 218–226. https://doi.org/10.1016/j.cej.2014.01.061.
(17) Liu, Y.; Ptacek, C. J.; Baldwin, R. J.; Cooper, J. M.; Blowes, D. W. Application of Zero-Valent Iron Coupled with Biochar for Removal of Perfluoroalkyl Carboxylic and Sulfonic Acids from Water under Ambient Environmental Conditions. *Sci. Total Environ.* **2020**, *719*, 137372. https://doi.org/10.1016/j.scitotenv.2020.137372.
(18) Garg, R.; Mittal, M.; Tripathi, S.; Eddy, N. O. Core to Concept: Synthesis, Structure, and Reactivity of Nanoscale Zero-Valent Iron (NZVI) for Wastewater Remediation. *Environ. Sci. Pollut. Res.* **2024**, *31* (60), 67496–67520. https://doi.org/10.1007/s11356-024-33197-x.
(19) Xu, B.-D.; Li, D.-C.; Qian, T.-T.; Jiang, H. Boosting the Activity and Environmental Stability of Nanoscale Zero-Valent Iron by Montmorillonite Supporting and Sulfidation Treatment. *Chem. Eng. J.* **2020**, *387*, 124063. https://doi.org/10.1016/j.cej.2020.124063.
(20) Gao, R.; Hu, P.; Dai, Y.; Zhang, Y.; Liu, L.; Yang, W. Removal of Cadmium(II) from Aqueous Solutions by a Novel Sulfide-Modified Nanoscale Zero-Valent Iron Supported on Kaolinite: Treatment Efficiency, Kinetics and Mechanisms. *Appl. Surf. Sci.* **2022**, *602*, 154353. https://doi.org/10.1016/j.apsusc.2022.154353.
(21) Liu, X.; Wang, Q.; Zhang, Z.; Jia, L.; Shen, Z.; Long, T.; Chen, G. Z.; He, J.; Song, X. Immobilizing S-nZVI@LDO for Simultaneous Removal of PFOA and TCE Co-Contaminants from Groundwater. *J. Hazard. Mater.* **2025**, *495*, 138949. https://doi.org/10.1016/j.jhazmat.2025.138949.
(22) Zhang, Y.-Y.; Jiang, H.; Zhang, Y.; Xie, J.-F. The Dispersity-Dependent Interaction between Montmorillonite Supported nZVI and Cr(VI) in Aqueous Solution. *Chem. Eng. J.* **2013**, *229*, 412–419. https://doi.org/10.1016/j.cej.2013.06.031.
(23) Abollino, O.; Aceto, M.; Malandrino, M.; Sarzanini, C.; Mentasti, E. Adsorption of Heavy Metals on Na-Montmorillonite. Effect of pH and Organic Substances. *Water Res.* **2003**, *37*

(7), 1619–1627. https://doi.org/10.1016/S0043-1354(02)00524-9.
(24) Lei, X.; Lian, Q.; Zhang, X.; Karsili, T. K.; Holmes, W.; Chen, Y.; Zappi, M. E.; Gang, D. D. A Review of PFAS Adsorption from Aqueous Solutions: Current Approaches, Engineering Applications, Challenges, and Opportunities. *Environ. Pollut.* **2023**, *321*, 121138. https://doi.org/10.1016/j.envpol.2023.121138.
(25) Wang, J.; Chen, C.; Jeanne Huang, J.; Xiao, N.; Li, S. Synchronous or Selective Removal of Nitrate and Cr(VI) by Montmorillonite Supported Sulfidized Nanoscale Zerovalent Iron: Role of Fe(II) and S0. *Sep. Purif. Technol.* **2025**, *354*, 129006. https://doi.org/10.1016/j.seppur.2024.129006.
(26) Lv, D.; Zhou, X.; Zhou, J.; Liu, Y.; Li, Y.; Yang, K.; Lou, Z.; Baig, S. A.; Wu, D.; Xu, X. Design and Characterization of Sulfide-Modified Nanoscale Zerovalent Iron for Cadmium(II) Removal from Aqueous Solutions. *Appl. Surf. Sci.* **2018**, *442*, 114–123. https://doi.org/10.1016/j.apsusc.2018.02.085.
(27) Ruan, J.; Tang, T.; Zhang, M.; Qiao, W. Interaction Mechanism between Chlorinated Polyfluoroalkyl Ether Potassium Sulfonate (F–53B) and Chromium on Different Types of Soil Surfaces. *Environ. Pollut.* **2022**, *311*, 119820. https://doi.org/10.1016/j.envpol.2022.119820.
(28) Gao, Y.; Deng, S.; Du, Z.; Liu, K.; Yu, G. Adsorptive Removal of Emerging Polyfluoroalky Substances F-53B and PFOS by Anion-Exchange Resin: A Comparative Study. *J. Hazard. Mater.* **2017**, *323*, 550–557. https://doi.org/10.1016/j.jhazmat.2016.04.069.
(29) Ma, M.; Coulon, F.; Tang, Z.; Hu, Z.; Bi, Y.; Huo, M.; Song, X. Unveiling the Truth of Interactions between Microplastics and Per- and Polyfluoroalkyl Substances (PFASs) in Wastewater Treatment Plants: Microplastics as a Carrier of PFASs and Beyond. *Environ. Sci. Technol.* **2025**, *59* (4), 2211–2221. https://doi.org/10.1021/acs.est.4c08898.
(30) Tang, Z.; Song, X.; Xu, M.; Yao, J.; Ali, M.; Wang, Q.; Zeng, J.; Ding, X.; Wang, C.; Zhang, Z.; Liu, X. Effects of Co-Occurrence of PFASs and Chlorinated Aliphatic Hydrocarbons on Microbial Communities in Groundwater: A Field Study. *J. Hazard. Mater.* **2022**, *435*, 128969. https://doi.org/10.1016/j.jhazmat.2022.128969.
(31) Xu, J.; Cao, Z.; Wang, Y.; Zhang, Y.; Gao, X.; Ahmed, M. B.; Zhang, J.; Yang, Y.; Zhou, J. L.; Lowry, G. V. Distributing Sulfidized Nanoscale Zerovalent Iron onto Phosphorus-Functionalized Biochar for Enhanced Removal of Antibiotic Florfenicol. *Chem. Eng. J.* **2019**, *359*, 713–722. https://doi.org/10.1016/j.cej.2018.11.180.
(32) Hanaor, D.; Michelazzi, M.; Leonelli, C.; Sorrell, C. C. The Effects of Carboxylic Acids on the Aqueous Dispersion and Electrophoretic Deposition of ZrO_2. *J. Eur. Ceram. Soc.* **2012**, *32* (1), 235–244. https://doi.org/10.1016/j.jeurceramsoc.2011.08.015.
(33) Ravikovitch, P. I.; Neimark, A. V. Characterization of Nanoporous Materials from Adsorption and Desorption Isotherms. *Colloids Surf. Physicochem. Eng. Asp.* **2001**, *187–188*, 11–21. https://doi.org/10.1016/S0927-7757(01)00614-8.
(34) Kovalchuk, I.; Kornilovych, B.; Tobilko, V.; Bondarieva, A.; and, Y. K. Adsorption Removal of Heavy Metal Ions from Multi-Component Aqueous System by Clay-Supported Nanoscale Zero-Valent Iron. *J. Dispers. Sci. Technol.* **2023**, *45* (1), 68–79. https://doi.org/10.1080/01932691.2022.2127754.
(35) Zhang, J.; Zhang, N.; Tack, F. M. G.; Sato, S.; Alessi, D. S.; Oleszczuk, P.; Wang, H.; Wang, X.; Wang, S. Modification of Ordered Mesoporous Carbon for Removal of Environmental

Contaminants from Aqueous Phase: A Review. *J. Hazard. Mater.* **2021**, *418*, 126266. https://doi.org/10.1016/j.jhazmat.2021.126266.

(36) Jiang, J.-Q.; Zeng, Z. Comparison of Modified Montmorillonite Adsorbents: Part II: The Effects of the Type of Raw Clays and Modification Conditions on the Adsorption Performance. *Chemosphere* **2003**, *53* (1), 53–62. https://doi.org/10.1016/S0045-6535(03)00449-1.

(37) Bhowmick, S.; Chakraborty, S.; Mondal, P.; Renterghem, W. V.; Berghe, S. V. den; Roman-Ross, G.; Chatterjee, D.; Iglesias, M. Montmorillonite-Supported Nanoscale Zero-Valent Iron for Removal of Arsenic from Aqueous Solution: Kinetics and Mechanism. *Chem. Eng. J.* **2014**, *243*, 14–23. https://doi.org/10.1016/j.cej.2013.12.049.

(38) Wu, D.; Peng, S.; Yan, K.; Shao, B.; Feng, Y.; Zhang, Y. Enhanced as(III) Sequestration Using Sulfide-Modified Nano-Scale Zero-Valent Iron with a Characteristic Core–Shell Structure: Sulfidation and as Distribution. *ACS Sustain. Chem. Eng.* **2018**, *6* (3), 3039–3048. https://doi.org/10.1021/acssuschemeng.7b02787.

(39) Dong, H.; Zhang, C.; Deng, J.; Jiang, Z.; Zhang, L.; Cheng, Y.; Hou, K.; Tang, L.; Zeng, G. Factors Influencing Degradation of Trichloroethylene by Sulfide-Modified Nanoscale Zero-Valent Iron in Aqueous Solution. *Water Res.* **2018**, *135*, 1–10. https://doi.org/10.1016/j.watres.2018.02.017.

(40) Kim, E.-J.; Kim, J.-H.; Azad, A.-M.; Chang, Y.-S. Facile Synthesis and Characterization of Fe/FeS Nanoparticles for Environmental Applications. *ACS Appl. Mater. Interfaces* **2011**, *3* (5), 1457–1462. https://doi.org/10.1021/am200016v.

(41) Yamashita, T.; Hayes, P. Analysis of XPS Spectra of Fe2+ and Fe3+ Ions in Oxide Materials. *Appl. Surf. Sci.* **2008**, *254* (8), 2441–2449. https://doi.org/10.1016/j.apsusc.2007.09.063.

(42) Borgnino, L.; Avena, M. J.; Pauli, C. P. D. Synthesis and Characterization of Fe(III)-Montmorillonites for Phosphate Adsorption. *Colloids Surf. Physicochem. Eng. Asp.* **2009**, *341* (1), 46–52. https://doi.org/10.1016/j.colsurfa.2009.03.037.

(43) Wu, Y.; Zou, Y.; Liu, X.; Wang, B.; Li, R.; Liu, Y.; Chi, Z.; Wu, S.; Deng, M. Rapid Removal of 6:2 Chlorinated Polyfluorinated Ether Sulfonate from Water by Sludge-Based Biochar: Performance and Mechanism. *J. Water Process Eng.* **2025**, *69*, 106794. https://doi.org/10.1016/j.jwpe.2024.106794.

(44) Xu, J.; Avellan, A.; Li, H.; Liu, X.; Noël, V.; Lou, Z.; Wang, Y.; Kaegi, R.; Henkelman, G.; Lowry, G. V. Sulfur Loading and Speciation Control the Hydrophobicity, Electron Transfer, Reactivity, and Selectivity of Sulfidized Nanoscale Zerovalent Iron. *Adv. Mater.* **2020**, *32* (17), 1906910. https://doi.org/10.1002/adma.201906910.

(45) Reis, A. S.; Ardisson, J. D. Exchangeable Ion and Thermal Treatment Effects on Basal Spacings of Al-Hydroxy Pillared Montmorillonites. *Clays Clay Miner.* **2003**, *51* (1), 33–40. https://doi.org/10.1346/CCMN.2003.510104.

(46) Zhao, S.; Liu, S.; Wang, F.; Lu, X.; Li, Z. Sorption Behavior of 6:2 Chlorinated Polyfluorinated Ether Sulfonate (F-53B) on Four Kinds of Nano-Materials. *Sci. Total Environ.* **2021**, *757*, 144064. https://doi.org/10.1016/j.scitotenv.2020.144064.

(47) Ismail, B.; Hussain, S. T.; Akram, S. Adsorption of Methylene Blue onto Spinel Magnesium Aluminate Nanoparticles: Adsorption Isotherms, Kinetic and Thermodynamic Studies. *Chem. Eng. J.* **2013**, *219*, 395–402. https://doi.org/10.1016/j.cej.2013.01.034.

(48) Gong, Y.; Wang, Y.; Lin, N.; Wang, R.; Wang, M.; Zhang, X. Iron-Based Materials for

Simultaneous Removal of Heavy Metal(Loid)s and Emerging Organic Contaminants from the Aquatic Environment: Recent Advances and Perspectives. *Environ. Pollut.* **2022**, *299*, 118871. https://doi.org/10.1016/j.envpol.2022.118871.

(49) Wei, X.; Guo, Z.; Yin, H.; Yuan, Y.; Chen, R.; Lu, G.; Dang, Z. Removal of Heavy Metal Ions and Polybrominated Biphenyl Ethers by Sulfurized Nanoscale Zerovalent Iron: Compound Effects and Removal Mechanism. *J. Hazard. Mater.* **2021**, *414*, 125555. https://doi.org/10.1016/j.jhazmat.2021.125555.

(50) Liu, T.; Li, X.; Waite, T. D. Depassivation of Aged Fe0 by Divalent Cations: Correlation between Contaminant Degradation and Surface Complexation Constants. *Environ. Sci. Technol.* **2014**, *48* (24), 14564–14571. https://doi.org/10.1021/es503777a.

(51) Mu, C.; Zhu, C.; Wang, D.; Huang, D.; Zhou, D. Role of Activated Carbon in Hydroxyl Radical Production and Secondary Mineral Formation during Iron Sulfide (FeS) Oxidation. *Environ. Sci. Technol.* **2025**, *59* (31), 16452–16462. https://doi.org/10.1021/acs.est.5c06235.

(52) Dong, Q.; Min, X.; Huo, J.; Wang, Y. Efficient Sorption of Perfluoroalkyl Acids by Ionic Liquid-Modified Natural Clay. *Chem. Eng. J. Adv.* **2021**, *7*, 100135. https://doi.org/10.1016/j.ceja.2021.100135.

(53) Vu, C. T.; Wu, T. Adsorption of Short-Chain Perfluoroalkyl Acids (PFAAs) from Water/Wastewater. *Env. Sci Water Res Technol* **2020**, *6* (11), 2958–2972. https://doi.org/10.1039/D0EW00468E.

(54) Yu, H.; Chen, H.; Fang, B.; Sun, H. Sorptive Removal of Per- and Polyfluoroalkyl Substances from Aqueous Solution: Enhanced Sorption, Challenges and Perspectives. *Sci. Total Environ.* **2023**, *861*, 160647. https://doi.org/10.1016/j.scitotenv.2022.160647.

(55) Zhang, Y.; Thomas, A.; Apul, O.; Venkatesan, A. K. Coexisting Ions and Long-Chain per- and Polyfluoroalkyl Substances (PFAS) Inhibit the Adsorption of Short-Chain PFAS by Granular Activated Carbon. *J. Hazard. Mater.* **2023**, *460*, 132378. https://doi.org/10.1016/j.jhazmat.2023.132378.

(56) Mahofa, E.; El Meragawi, S.; Vilayatteri, M. A.; Dwivedi, S.; Panda, M. R.; Jovanović, P.; van Duin, A. C. T.; Freeman, B.; Tanksale, A.; Majumder, M. Manipulating Intrapore Energy Barriers in Graphene Oxide Nanochannels for Targeted Removal of Short-Chain PFAS. *ACS Nano* **2025**, *19* (15), 14742–14755. https://doi.org/10.1021/acsnano.4c15413.

(57) Hayati-Ashtiani, M. Use of FTIR Spectroscopy in the Characterization of Natural and Treated Nanostructured Bentonites (Montmorillonites). *Part. Sci. Technol.* **2012**, *30* (6), 553–564. https://doi.org/10.1080/02726351.2011.615895.

(58) Zhao, L.; Bian, J.; Zhang, Y.; Zhu, L.; Liu, Z. Comparison of the Sorption Behaviors and Mechanisms of Perfluorosulfonates and Perfluorocarboxylic Acids on Three Kinds of Clay Minerals. *Chemosphere* **2014**, *114*, 51–58. https://doi.org/10.1016/j.chemosphere.2014.03.098.

(59) Wang, M.; Orr, A. A.; Jakubowski, J. M.; Bird, K. E.; Casey, C. M.; Hearon, S. E.; Tamamis, P.; Phillips, T. D. Enhanced Adsorption of Per- and Polyfluoroalkyl Substances (PFAS) by Edible, Nutrient-Amended Montmorillonite Clays. *Water Res.* **2021**, *188*, 116534. https://doi.org/10.1016/j.watres.2020.116534.

(60) Su, Y.; Adeleye, A. S.; Keller, A. A.; Huang, Y.; Dai, C.; Zhou, X.; Zhang, Y. Magnetic Sulfide-Modified Nanoscale Zerovalent Iron (S-nZVI) for Dissolved Metal Ion Removal. *Water Res.* **2015**, *74*, 47–57. https://doi.org/10.1016/j.watres.2015.02.004.

(61) Tang, X.; Luan, Y.; Zhao, Y.; Li, B.; Wu, M.; Lai, Y. Tetrasodium Iminodisuccinate Modified Montmorillonite for Pb and Cd Adsorption from Water: Characterization and Mechanism. *J. Environ. Chem. Eng.* **2024**, *12* (5), 113953. https://doi.org/10.1016/j.jece.2024.113953.

(62) Zhou, Q.; Deng, S.; Yu, Q.; Zhang, Q.; Yu, G.; Huang, J.; He, H. Sorption of Perfluorooctane Sulfonate on Organo-Montmorillonites. *Chemosphere* **2010**, *78* (6), 688–694. https://doi.org/10.1016/j.chemosphere.2009.12.005.

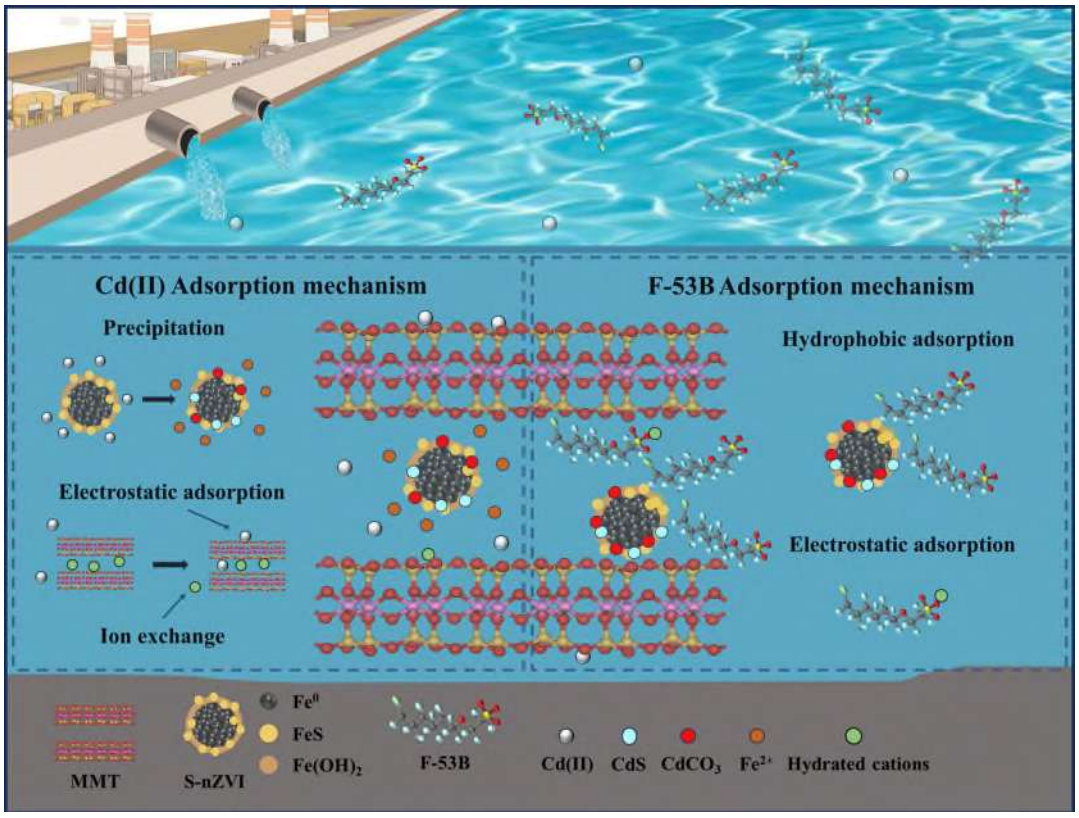
(63) Tian, S.; Gong, Y.; Ji, H.; Duan, J.; Zhao, D. Efficient Removal and Long-Term Sequestration of Cadmium from Aqueous Solution Using Ferrous Sulfide Nanoparticles: Performance, Mechanisms, and Long-Term Stability. *Sci. Total Environ.* **2020**, *704*, 135402. https://doi.org/10.1016/j.scitotenv.2019.135402.

(64) Liu, H.; Lyu, H.; Zhang, W.; Jiang, J.; Li, X.; Xue, S. Surfactant-Modified SiO_2/FeS Nanocomposites for Remediation of Cadmium Pollution. *J. Cent. South Univ.* **2024**, *31* (4), 1163–1177. https://doi.org/10.1007/s11771-024-5605-8.

(65) Sühnholz, S.; Gawel, A.; Kopinke, F.-D.; Mackenzie, K. Evidence of Heterogeneous Degradation of PFOA by Activated Persulfate – FeS as Adsorber and Activator. *Chem. Eng. J.* **2021**, *423*, 130102. https://doi.org/10.1016/j.cej.2021.130102.

892

Graphical abstract



893



https://dspace.org/

Co-removal of cadmium and F-53B from aqueous solutions using montmorillonite-supported sulfidated nZVI: performance and mechanistic insights

Wang, Qing; Zhou, Yi; Jia, Liangchun; Coulon, Frederic; Dong, Changxun ...

2026-01-09
American Chemical Society (ACS)
https://doi.org/10.1021/acsestwater.5c01073
Wang Q, Zhou Y, Jia L, et al., (2026) Co-removal of cadmium and F-53B from aqueous solutions using montmorillonite-supported sulfidated nZVI: performance and mechanistic insights. ACS ES&T Water, Volume 6, Issue 1, January 2026, pp. 341-354

Downloaded from a DSpace repository. https://dspace.org/